



*Cent. Eur. J. Energ. Mater.* 2024, 21(4): 450-481; DOI 10.22211/cejem/198429

Article is available in PDF-format, in colour, at:

<https://ipo.lukasiewicz.gov.pl/wydawnictwa/cejem-woluminy/vol-21-nr-4/>



Article is available under the Creative Commons Attribution-NonCommercial-NoDerivs 3.0 license CC BY-NC-ND 3.0.

*Research paper*

## Theoretical Analysis and Numerical Study for Spin Jet Formation Performance

Shengjie Sun<sup>1)</sup>, Shuyou Wang<sup>1,2,\*</sup>, Jianwei Jiang<sup>1)</sup>,  
Zhaoting Li<sup>1)</sup>, Hang Yang<sup>1)</sup>, Jianbing Men<sup>1,2)</sup>

<sup>1)</sup> National Key Laboratory of Explosion Science and Safety Protection, Beijing Institute of Technology, Beijing 100081, PR China

<sup>2)</sup> Tangshan Research Institute, Beijing Institute of Technology, Tangshan 063000, Hebei, China

\* E-mail: wangsy@bit.edu.cn

**Abstract:** Small-caliber shaped charges rely on rotation for flight stability; however, this rotation impacts the jet formation performance, leading to radial dispersion and fragmentation of the jet. This study establishes a theoretical model to analyse the rotating jet formation process, based on classical jet formation theory. A smoothed particle hydrodynamics (SPH) numerical simulation model, calibrated with existing experimental data, was employed to simulate the formation process of rotating jets, and revealed the interplay between the jet's axial and tangential velocities. Based on these findings, a theoretical analysis model for rotating jet formation was developed under specific assumptions to predict the jet velocity distribution, jet radius distribution, and fracture time. The theoretical results indicate that regardless of the initial angular velocity, the jet does not fracture instantaneously; on the contrary, it fractures progressively from the tip to the tail. The discrepancies between theoretical predictions and numerical simulations for the jet tip velocity and fracture time were 4.2% and 4.2  $\mu$ s, respectively, validating the accuracy of the theoretical model.

**Keywords:** shaped charge, jet formation theory, rotating jet, numerical simulation

## 1 Introduction

Due to the need for small-caliber ammunition to rely on spin for flight stability, the cohesiveness of the jet formed by the shaped charge liner is compromised when the high-speed rotating projectile impacts the target, leading to a sharp decrease in the jet's penetration power. This phenomenon was initially investigated by Simon in 1943 and subsequently studied by Schall and Thomer, who utilized flash X-ray photography to observe the formation dynamics of spinning jets [1]. The results demonstrated an increase in jet radius due to rotation, while the axial velocity of the jet remained unaffected by its angular velocity. Typically, the initial angular velocity of shaped charges ranges between 30 and 250 r/s [2]. At angular velocities below 30 r/s, the impact of rotation on jet penetration is negligible. Conversely, at an angular velocity of 30,000 r/s, the integrity of the jet is severely compromised due to substantial centrifugal stresses generated within the jet material [3], leading to fragmentation and a consequent reduction in penetration efficiency. In 1958, Singh developed a theoretical model to describe this effect, the results of which showed that the formation of a spinning jet involves both axial and tangential velocity components [4]. This induces an asymmetric collapse of the shaped charge liner, resulting in radial expansion of the jet. When the centrifugal stress exceeds the material's tensile limit, the jet disintegrates into fragments. However, the parameters employed in Singh's model were specific to a particular jet geometry, thus limiting the model's generalizability. Meanwhile, based on Singh's theory, Segletes conducted a theoretical analysis of the stress in a rotating jet during the elongation process, and demonstrated that the tangential and axial motions of the jet can be studied independently [5].

In order to gain a comprehensive understanding of centrifugal stress effects on jet formation, Marinko *et al.* [6] utilized the HYDRO simulation system to calculate stress distributions within a rotating jet, modelling it as an elastic bar. The simulation results were subsequently verified through experimental results. Similarly, Li *et al.* [7], conducted related studies, and showed that with increasing spin velocity, the jet tip velocity decreases slightly, while the jet radius decreases rather than expands. They suggested that this phenomenon encourages jet fragmentation, which negatively impacts penetration performance.

In light of current research, the radial scattering behaviour of rotating jets and its underlying mechanisms have been discussed extensively. The present study aimed to develop a theoretical model for analysing the rotating jet formation process, based on classical jet formation theory. Through this approach, the morphological characteristics and fracture behaviour of rotating jets were theoretically examined. As rotating jet formation involves both axial stretching

and circumferential rotation, this paper firstly presents a simulation study exploring jet formation under varying initial angular velocities. This simulation clarified the influence of the jet's axial motion on its circumferential behaviour. Based on these findings, relevant assumptions are proposed to enhance the theoretical understanding of rotating jet formation.

## 2 Materials and Methods

Although some discrepancies may arise between numerical simulation results and actual experimental outcomes, numerical simulation remains a foundational approach in experimental analysis. It not only allows for the computation of core physical laws but also provides insights into localized aspects of physical processes, making it an effective tool for examining transient nonlinear interactions [8]. Consequently, this study employs numerical simulation to validate the theoretical results of jet formation across varying initial angular velocities.

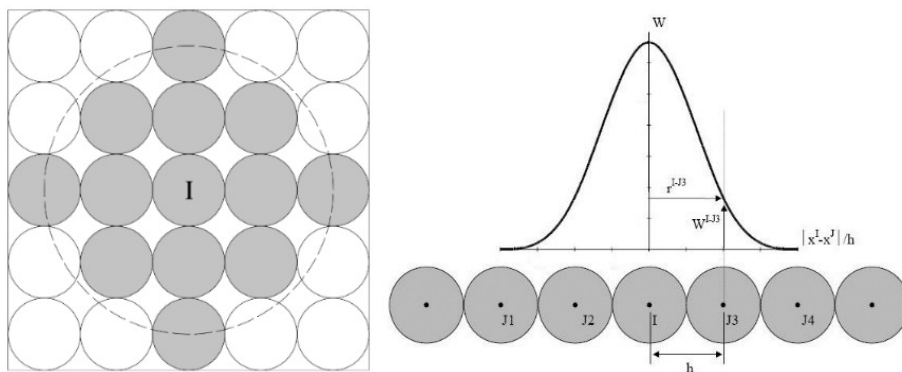
### 2.1 Numerical simulation model

Classical numerical simulation methods, notably the Eulerian and Lagrangian approaches, have seen widespread application in computational fluid dynamics and solid mechanics, serving as foundational techniques for spatial and numerical discretization [8]. However, the Eulerian approach struggles with irregular or complex geometries, often requiring intensive computational resources due to the need for detailed grid transformations. Additionally, accurately tracking free surfaces, deforming boundaries, and heterogeneous materials necessitates finer grids, further increasing computational demands. Similarly, the Lagrangian method is effective for many problems but faces severe grid distortion under extreme dynamic loads, such as explosions and high-speed impacts, limiting its precision and stability in such cases.

#### 2.1.1 Smoothed Particle Hydrodynamics (SPH) algorithm

In recent years, meshless methods have demonstrated unique advantages in various applications. Numerous studies have shown that using the SPH method to simulate explosive impacts [9, 10] and shaped charges [11, 12] yields numerical results that closely match experimental observations. This algorithm effectively mitigates challenges such as grid distortion, high non-uniformity, and complex interfaces between moving materials, and it has been widely applied in the study of material response under high dynamic loads and fluid dynamics problems involving large deformations [13].

In the SPH algorithm, objects are discretized into particles, each with properties such as mass, coordinates, velocity, and internal energy. Particle interactions are modelled using smoothing kernel functions, as shown in Figure 1.



**Figure 1.** Schematic diagram of the SPH kernel function principle

Taking density as an example, the density expression at particle  $I$  is:

$$\rho_I = \sum_{J=1}^N m^J W^{IJ} (X^I - X^J, h) \quad (1)$$

where  $m_j$  is the mass of particle  $J$ ,  $W_{IJ}$  is the kernel function,  $X$  is the centre position of the particle, and  $h$  is the smoothing length. When performing solution calculations, the smoothing length of the SPH method must also be defined. The smoothing length defined in terms of time integration is shown in Equation 2 [14].

$$\frac{d}{dt}(h(t)) = \frac{1}{D} h(t) (\text{div}(v))^{1/3} \quad (2)$$

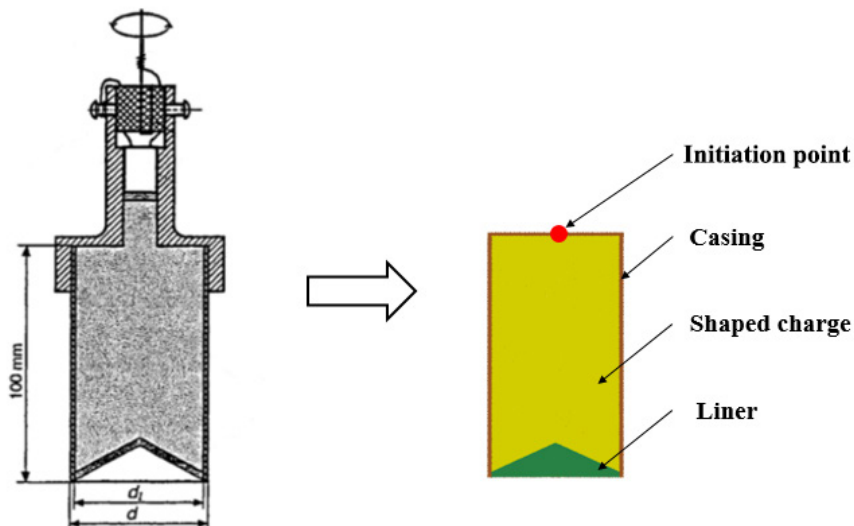
where  $h(t)$  denotes the smoothing length at moment  $t$ ,  $D$  represents the dimensionality of the computation (e.g. for a three-dimensional problem,  $D$  is set to 3), and  $v$  represents the physical quantity studied. Since the SPH algorithm operates inherently as a Lagrangian method and accurately captures fluid characteristics, it is particularly suitable for modelling the formation of energetic jets, which behave as highly plastic flow-state solids [15, 16]. Additionally, by employing smoothing kernel functions to model particle interactions, the SPH algorithm eliminates the need for grid or particle removal during fracture simulation. Instead, fractures are represented by assigning each

particle a weighting factor based on its interactions with adjacent particles. This approach not only prevents the mass loss commonly associated with grid removal in traditional Lagrangian fracture simulations but also addresses the strength inaccuracies found in Eulerian models when simulating material separation. As a result, the SPH method provides a more accurate representation of material fracture characteristics under high-temperature and high-strain conditions [17].

Given the advantages of the SPH method, the present study uses LS-DYNA nonlinear dynamic simulation software to model the formation of energetic jets, thereby validating theoretical conclusions. To accurately capture the effects of angular velocity on rotating jets, a three-dimensional algorithm is applied, with a complete model of the explosive charge and its liner included in the simulation.

### 2.1.2 Algorithm calibration

As in the Lagrangian approach, the accuracy of the SPH algorithm is highly sensitive to the number of particles used in the simulations. Therefore, this study initially addressed the particle quantity sensitivity. Feng *et al.* [11] as a frequently used form of explosive charge for military and industrial applications, can produce powerful metal jet and lead to stronger penetration effects onto targets than normal charges. After the explosion of high explosive (HE examined this aspect using a  $\Phi 48 \times 100$  mm TNT explosive charge and a 3 mm thick aluminium liner with a conical angle of  $60^\circ$ ). Their study employed two-dimensional SPH simulations to assess the effect of particle count on the computed results, and found that convergence in the jet tip velocity was achieved with 1,392 particles for the liner and 3,784 for the explosive charge. To ensure the validity of particle spacing and model parameters in the present study, the particle spacing was set at 0.375 mm. Based on the charge structure and operational conditions from previous studies [18], the formation of the rotating jet was computed, and the simulation results were compared to experimental data for model calibration. Figure 2 illustrates the validation model established for the SPH algorithm.



**Figure 2.** SPH algorithm verification model [18]

In 1968, Jones, Wilkins and Lee proposed the famous JWL equation of state to describe the diffusion process of detonation products [19]. The equation form is as follows:

$$P_b = C_1 \left( 1 - \frac{\omega}{r_1 v} \right) e^{-r_1 v} + C_2 \left( 1 - \frac{\omega}{r_2 v} \right) e^{-r_2 v} + \frac{\omega E}{v} \quad (3)$$

where  $P_b$  is the explosion pressure (in GPa),  $E$  is the initial energy per unit volume, and  $v$  is the initial specific volume.  $C_1$ ,  $C_2$ ,  $r_1$  and  $r_2$  are material constants. The charging parameters used in the numerical simulation were taken from the literature [20], as listed in Table 1.

**Table 1.** JWL parameters of the charge (TNT/RDX 50/50) [20]

Density [g/cm <sup>3</sup> ]	Detonation velocity [m/s]	C-J pressure [GPa]	$E_0$ [GPa]	$C_1$ [GPa]	$C_2$ [GPa]	$r_1$	$r_2$	$\omega$
1.64	7610	26	8.1	472.8	10.7	4.4	1.2	0.32

The liner material used was copper. Of the numerous constitutive equations, the Johnson-Cook model effectively describes the relationship between stress, strain, strain rate, and temperature, especially under high-temperature and

high-strain-rate conditions [21]. It is especially advantageous for modelling the dynamic behaviour of copper and its alloys [22]. Therefore, this study employs the Johnson-Cook constitutive equation to characterise the jet shaping process. The fundamental form of the Johnson-Cook constitutive equation is as follows:

$$\sigma = (A + B\varepsilon^n)(1 + C \ln \dot{\varepsilon}^*)(1 - T^{*m}) \quad (4)$$

where  $A$ ,  $B$ ,  $n$ ,  $C$ , and  $m$  are material constants that need calibration through experimental results.  $\sigma$  represents the equivalent stress,  $\varepsilon$  denotes the equivalent strain,  $\dot{\varepsilon}^*$  stands for the dimensionless strain rate,  $T^* = (T - T_r)/(T_m - T_r)$ ,  $T$  signifies the material temperature,  $T_r$  denotes room temperature, and  $T_m$  represents the material's melting point. According to the research by Johnson and Cook, the stress triaxiality  $\sigma^*$ , strain rate  $\dot{\varepsilon}^*$ , and temperature  $T$  simultaneously influence the dynamic failure strain of a material.

$$\varepsilon_f = [D_1 + D_2 \exp(D_3 \cdot \sigma^*)][1 + D_4 \cdot \ln \dot{\varepsilon}^*][1 + D_5 \cdot T^*] \quad (5)$$

where  $\sigma^*$  is the stress triaxiality, which can be calculated by dividing the average value of the three principal strains by the equivalent strain, as shown in Equation 6 [23]:

$$\sigma^* = \frac{\sigma_m}{\sigma_{eq}} \quad (6)$$

where  $\sigma_m$  is the average value of the principal stress of the material, that is:

$$\sigma_m = \frac{1}{3}(\sigma_1 + \sigma_2 + \sigma_3) \quad (7)$$

The material parameters of copper were taken from the literature [24], as listed in Table 2.

**Table 2.** Johnson-Cook model parameters of copper [24]

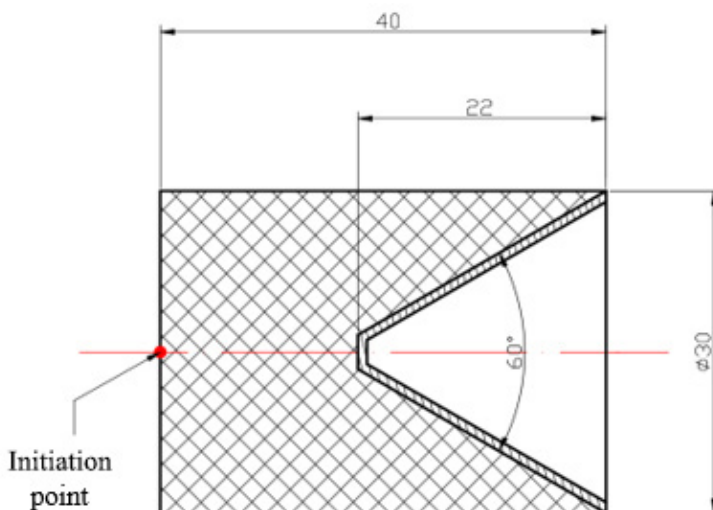
Density [g/cm <sup>3</sup> ]	$A$ [MPa]	$B$ [MPa]	$n$	$C$	$m$
8.96	90	292	0.31	0.025	1.09
$T_m$ [K]	$D1$	$D2$	$D3$	$D4$	$D5$
1356	0.54	4.89	-3.03	0.014	1.12

The \*INITIAL\_VELOCITY\_GENERATION keyword was used to apply an initial angular velocity (in radians) to the warhead. The jet formation morphologies at 55 and 84  $\mu\text{s}$  post-initiation were then computed and compared with experimental data from the literature, as depicted in Figure 3.

This figure illustrates that, under rotational conditions, the penetrator undergoes radial expansion and fracture. These behaviours are well captured in the numerical simulations, showing a high degree of similarity with experimental observations. This comparison confirms that the SPH algorithm simulates effectively the jet formation morphology and fracture phenomena. Consequently, this study will use the established numerical model to investigate the jet shaping processes across varying initial angular velocities.

### 2.1.3 Numerical simulation model for spinning jet study

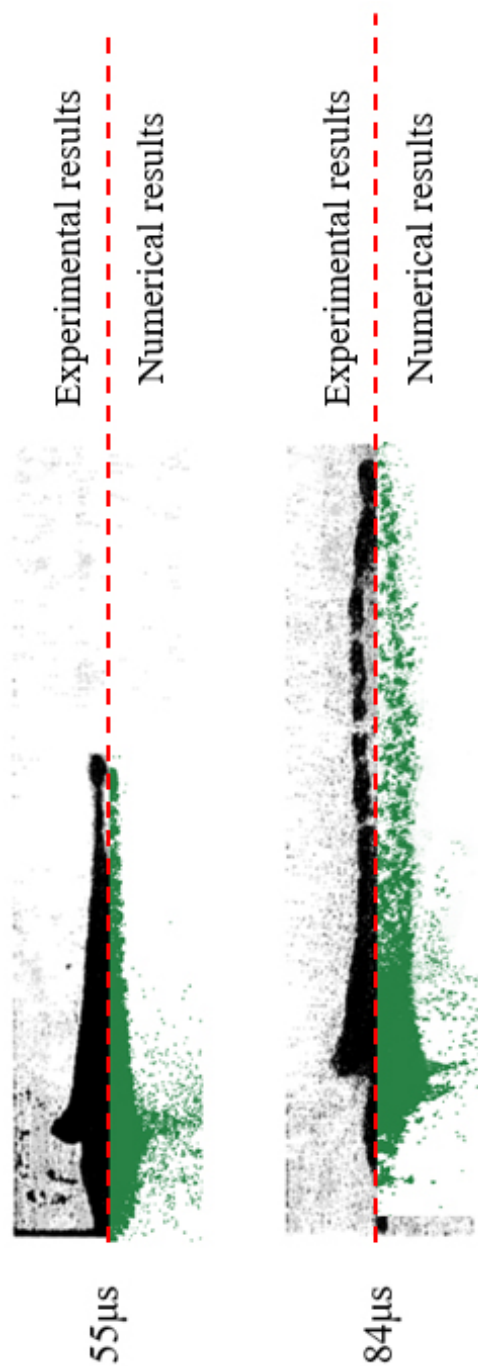
Based on the calibrated numerical simulation model, a 30 mm calibre shaped charge structure was used, as shown in Figure 4, to study the formation characteristics of the rotating jet. The liner thickness used was 1 mm, with 3 to 4 layers of particles staggered in the thickness direction.



**Figure 4.** Schematic diagram of the 30 mm calibre charge structure

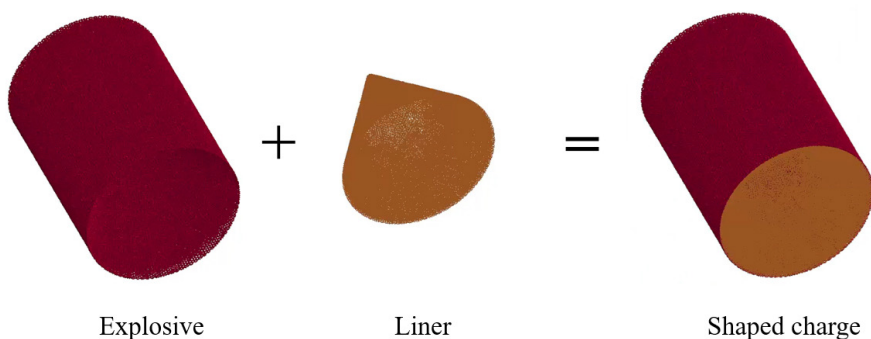
In order to improve the computational efficiency, the particle spacing between the liner's outer surface and the inner surface of the explosive charge was set to 0.375 mm. A gradient particle spacing was then applied, increasing to 0.5 mm towards the charge boundary. The model comprised a total of 906,440





**Figure 3.** Comparison of the numerical simulation and experimental results of rotating jet formation [17]

SPH particles, including 121,904 particles for the liner and 784,536 particles for the charge respectively. The discretized SPH model established is illustrated in Figure 5.



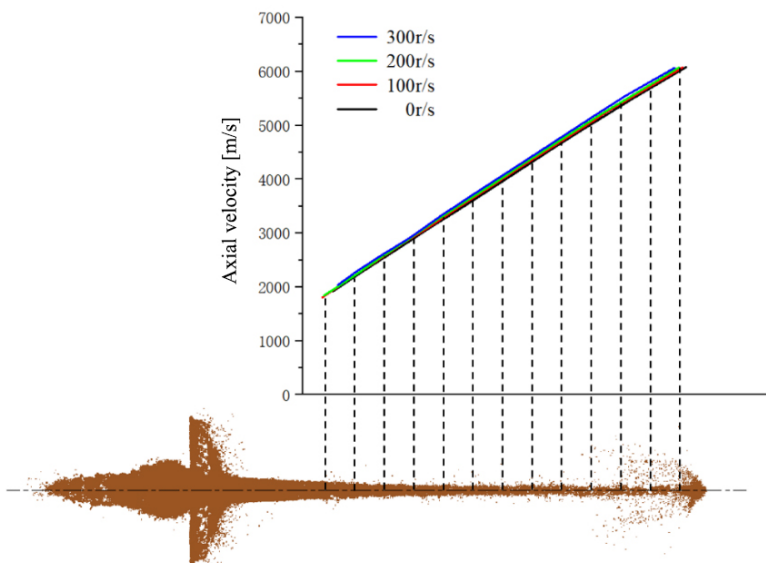
**Figure 5.** Shaped charge SPH discretization model

At 25  $\mu\text{s}$  after charge initiation, the jet velocity distribution contours under different initial angular velocities were extracted, as shown in Table 3.

**Table 3.** Velocity distribution cloud diagram of the rotating jet at 25  $\mu\text{s}$  after charge initiation.

Label	Initial angular velocity (r/s)	Jet axial velocity distribution contour
Axial velocity (m/s) 6500 6175 5850 5525 5200 4875 4550 4225 3900 3575 3250 2925 2600 2275 1950 1625 1300 970 650 325 0	0	
	100	
	200	
	300	

For varying initial angular velocities, the jet's axial velocity distribution showed no significant differences. Axial velocities for each jet were measured at 25  $\mu\text{s}$ , with the data presented in Figure 6.



**Figure 6.** Jet axial velocity distribution for different initial angular velocities

Figure 6 demonstrates that, across different initial angular velocities, the jet's axial velocity distribution remains similar, especially for initial velocities of 0 and 100 r/s, where the maximum difference in jet tip velocity is only 3.2%. Thus, this study considers the jet's rotational and axial motions as independent phenomena, assuming that rotational motion does not affect axial motion. Based on this assumption, a theoretical analysis of the rotating jet formation process was conducted.

## 2.2 Theoretical model of the rotating jet formation process

For conventional jets, circumferential motion is typically disregarded during the shaping process, allowing a two-dimensional axisymmetric model to suffice. However, under rotational conditions, the jet's internal stresses include both centrifugal and tangential components in addition to axial stress. These stresses are primarily influenced by the liner's initial angular velocity and the radius changes of jet elements between initial and final states. Furthermore, jet fracture timing is critical in characterizing the jet formation process. In order to analyze the fracture behaviour of a rotating jet, it is essential to derive the

jet's stress and strain distributions based on classical jet formation theory. The present study extends the two-dimensional axisymmetric jet formation theory to a three-dimensional framework, enabling calculation of radius, stress, and strain distributions in the rotating jet over time. This approach aimed to predict the fracture time and location for a conventional liner under rotational conditions.

### 2.2.1 Jet axial velocity distribution

In early 1983, Chou *et al.* [25] analysed a cross section of the internal explosive structure as a control volume and improved upon the Gruneisen equation of state [26]. They proposed an initial velocity prediction model for surface elements under implosive loading, which led to the derivation of the crushing velocity formula for the liner (Equation 8).

$$V_0 = \sqrt{2E} \cdot f(\mu', r_0 / r_i, I) \quad (8)$$

where  $\mu'$  is a constant to be calibrated,  $r_0$  and  $r_i$  are the outer and inner radii of the charge, and  $I$  represents the impulse of the charge on the liner. However, the parameter  $I$  in the equation requires fitting based on numerical simulation results, which limits the theoretical analysis of the liner's crushing process. To address this, Chanteret *et al.* [27] proposed a new theoretical assumption: during explosive detonation, a stationary cylindrical surface exists, where explosive products inside this surface drive the liner's crushing, while products outside diffuse outwards without contributing to the process. This assumption refines the initial implosion model, and the radius of the stationary cylindrical surface can be determined by solving Equation 9.

$$r_x^3 + 3 \cdot r_x \left[ (r_0 + r_i) \cdot \frac{\rho_e}{\rho_{CJ}} \cdot \left( \frac{M_i}{C} r_o + \frac{M_k}{C} r_i \right) + r_i \cdot r_0 \right] - 3 \cdot (r_i + r_0) \cdot r_i \cdot r_0 \cdot \left[ \frac{2}{3} + \frac{\rho_e}{\rho_{CJ}} \left( \frac{M_i}{C} + \frac{M_k}{C} \right) \right] = 0 \quad (9)$$

where  $M_i$  and  $M_k$  represent the mass per unit length of the liner and shell, respectively,  $r_i$  and  $r_0$  denote the inner and outer diameters of the charge, respectively, and  $\rho_e$  and  $\rho_{CJ}$  denote the initial density of the charge and the density of the products at the C-J interface, respectively. The density of the explosion products at the C-J interface can be calculated using Equation 10 [28].

$$\rho_{CJ} = \frac{K+1}{K} \rho_0 \quad (10)$$

where  $K$  represents the gas polytropic index. According to [28], an approximate value of  $K$  is taken as 1.4. In summary, the final formula (Equation 11) for calculating the crushing velocity of the liner is obtained as proposed by Chanteret *et al.* [27].

$$V_0 = \sqrt{\frac{2E}{\left(\frac{r_0^2 - r_i^2}{r_x^2 - r_i^2}\right) \cdot \frac{M_i}{C} + \frac{1}{6}}} \quad (11)$$

The initial crushing velocity of the liner decreases from top to bottom. To describe the effect of liner shape on the crushing angle, researchers such as Pugh, Eichelberger, and Rostoker developed an enhancement of Birkhoff's theory, referred to as the quasi-steady incompressible fluid mechanics theory, or PER theory [29]. Unlike Birkhoff's theory, the PER theory suggests that each liner element's crushing direction forms a non-perpendicular angle  $\delta$  with the liner's initial surface. This angle, known as the ejection angle, can be calculated using Equation 12 [29].

$$\delta = \arcsin \frac{V_0}{2 \cdot D \cdot \sec \alpha} \quad (12)$$

where  $V_0$  is the calculated initial crushing velocity of the charge cover,  $D$  is the charge detonation velocity, and  $\alpha$  is the half-cone angle of the charge cover. After calculating the projection angle, the distribution of the crushing angle  $\beta$  with respect to  $x$  can be calculated according to Equation 13 [29].

$$\tan \beta = \frac{\sin \alpha + 2 \cdot \sin \delta \cdot \cos(\alpha + \delta) - x \cdot \sin \alpha [1 - \tan(\alpha + \delta) \tan \delta] \cdot V_0' / V_0}{\cos \alpha - 2 \cdot \sin \delta \cdot \sin(\alpha + \delta) + x \cdot \sin \alpha [\tan(\alpha + \delta) + \tan \delta] V_0' / V_0} \quad (13)$$

According to the obtained projection angle  $\delta$  and crushing angle  $\beta$  of the liner, the expression for the jet velocity  $V_j$  can be derived [29], obtained in the form of Equation 14.

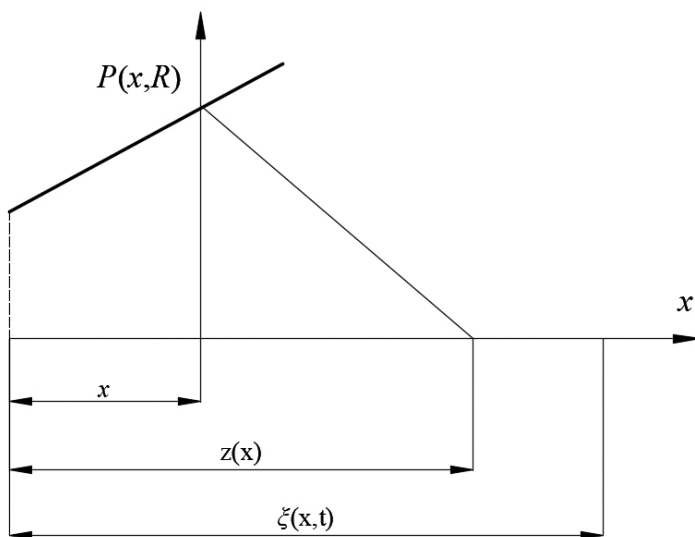
$$V_j = V_0 \csc \frac{\beta}{2} \cos \left( \alpha + \arcsin \frac{V_0}{2u_e} - \frac{\beta}{2} \right) \quad (14)$$

### 2.2.2 Jet radius distribution

Carleone and Chou introduced a Lagrangian coordinate system in which  $x$  represents the initial axial position of each jet element, and  $z(x)$  denotes the position where the liner element, originally at  $x$ , reaches the axis. This position is determined using Equation 15.

$$z(x) = x + R \cdot \tan(\alpha + \delta) \quad (15)$$

It is assumed that a given element reaches the axis at time  $t$ . Let  $\xi(x,t)$  represent the time-dependent axial position of the jet. The relationships between the variables are depicted in Figure 7.



**Figure 7.** Initial position  $x$  of jet element  $P$ , crushing position  $z$ , and positional movement  $\xi$  at time  $t$

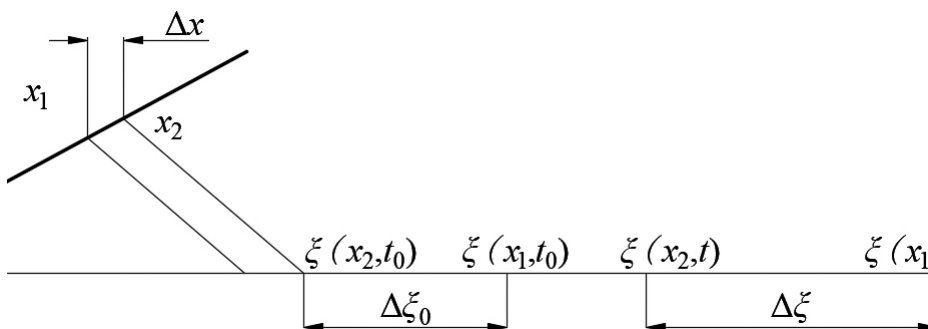
Assuming that each element reaches the axis at time  $t_c$  and that each element moves at a constant velocity  $V_j(x)$  immediately after reaching the axis, then at time  $t$ , the coordinate on the axis for the element at the initial position  $x$  is given by:

$$\xi(x,t) = z(x) + (t - t_c) \cdot V_j(x), \quad t \geq t_c \quad (16)$$

where  $t_c$  is determined as follows:

$$t_c = \frac{\sqrt{(z(x) - x)^2 + R^2}}{V_0(x)} \quad (17)$$

Two positions  $x_1$  and  $x_2$  on the liner were used to study the elongation process of the jet, as shown in Figure 8.



**Figure 8.** Schematic diagram of the elongation process of jet elements

During the crushing process, it is assumed that point  $x_1$  reaches the axis first to form the jet, and then point  $x_2$  reaches the axis at time  $t_0 = t_c(x_2)$ . At time  $t_0$ , the jet element at the initial position  $x_1$  reaches the location  $\xi(x_1, t_0)$ , while the jet element at the initial position  $x_2$  reaches the location  $\xi(x_2, t_0)$ . At time  $t$ , the positions of these two elements become  $\xi(x_1, t)$  and  $\xi(x_2, t)$ , respectively. According to the definition of strain, the one-dimensional strain of the jet can be defined as:

$$\varepsilon = \lim_{x_1 \rightarrow x_2} \frac{\Delta\xi - \Delta\xi_0}{\Delta\xi_0} = \lim_{x_1 \rightarrow x_2} \left[ \frac{\xi(x_2, t) - \xi(x_1, t)}{\xi(x_2, t_c(x_1)) - \xi(x_1, t_c(x_1))} \right] - 1 = \left[ \frac{\partial\xi}{\partial x}(x_1, t) / \frac{\partial\xi}{\partial x}(x_1, t_c(x_1)) \right] - 1 \quad (18)$$

For each of the liner elements:

$$\varepsilon(x, t) = \left[ \frac{\partial\xi}{\partial x}(x, t) / \frac{\partial\xi}{\partial x}(x, t_c(x)) \right] - 1 \quad (19)$$

The velocity gradient during jet elongation is the main contributor to axial stress in the jet. Assuming that the axial length of the casing element at the moment of axis collision represents the initial length of each jet segment, the strain expression for each jet segment at time  $t$  is given by Equation 20.

$$\varepsilon(x, t) = \lim_{\Delta t_0 \rightarrow 0} \frac{\Delta \xi(x) - \Delta l_0(x)}{\Delta l_0(x)}, t > t_c \quad (20)$$

The initial length of each jet element segment at the axis collision is:

$$\Delta l_0(x) = \Delta z(x) + V_j(x) \cdot \Delta t_c(x) \quad (21)$$

Then, based on the time increment  $\Delta t$ , the strain rate of each jet element at time  $t$  can be calculated:

$$\dot{\varepsilon}(x, t) = \frac{\varepsilon(x, t)}{\Delta t}, t \geq t_c \quad (22)$$

where the prime denotes differentiation with respect to  $x$ . Assuming a steady flow and incompressibility of the jet elements, the mass of the annular element with thickness  $b$  at position  $x$  is given by:

$$dm = 2\pi \cdot \rho_l \cdot b \cdot R \cdot dx / \cos \alpha \quad (23)$$

For a liner with a uniform wall thickness,  $R = x \tan \alpha$ . Since  $\frac{dm_j}{dm} = \sin^2 \beta$ , then:

$$\frac{dm_j}{dx} = \frac{2\pi \cdot \rho_l \cdot b \cdot R \cdot dx}{\cos \alpha} \cdot \sin^2 \beta \quad (24)$$

Assuming a circular cross section for the jet and constant density, with a cross-sectional radius of  $r_i$ , the mass of the jet element with length  $d\xi$  is:

$$\frac{dm_j}{dx} = \pi \cdot \rho_l \cdot r_i^2 \cdot \left| \frac{\partial \xi}{\partial x} \right| \quad (25)$$

Because  $d\xi$  and  $dx$  have opposite signs, the absolute value must be used when computing their ratio. Therefore, the expression for the radius of the jet element is derived as:



$$r_i = \left[ \frac{2xb \tan \alpha}{\cos \alpha} \cdot \frac{\sin^2(\beta/2)}{|\partial \xi / \partial x|} \right]^{1/2} \quad (26)$$

However, the above results describe the jet's radius variation only under conditions of zero initial angular velocity. When rotation is present, the jet radius expands radially due to centrifugal forces. The radial displacement  $u_j$  caused by the centrifugal stress on the jet can be calculated using Equation 27 [30].

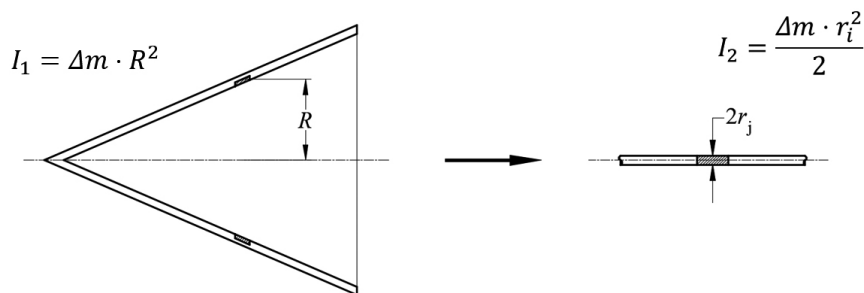
$$u_j = \frac{r_j^3(1+\nu)}{8E(1-\nu)} \cdot \rho_j \omega^2 \cdot \left[ \frac{3-5\nu}{1+\nu} - (1-2\nu) \right] \quad (27)$$

### 2.2.3 Breakup condition of the rotating jet

According to the principle of conservation of angular momentum, when the liner element forms the jet, the angular velocity  $\omega$  of the jet element at the axis can be expressed as:

$$\omega = \frac{2R^2}{r_j^2} \Omega \quad (28)$$

where  $\Omega$  is the initial angular velocity of the liner element.  $R$  and  $r_j$  are shown in Figure 9.



**Figure 9.** Schematic diagram of the morphology of the jet element before and after forming

Treating the jet as an equivalent cylindrical structure, based on the stress expressions for rotating cylinders, the radial stress  $\sigma_r$  and tangential stress  $\sigma_c$  of the jet element under rotation are calculated separately [30]:

$$\sigma_r = \frac{3-2\nu}{8(1-\nu)} \left( 1 - \frac{r^2}{r_j^2} \right) \rho_j \omega^2 r_j^2 \quad (29)$$

$$\sigma_c = \frac{3-2\nu}{8(1-\nu)} \left( 1 - 2 \cdot \frac{1+2\nu}{3-2\nu} \cdot \frac{r^2}{r_j^2} \right) \rho_j \omega^2 r_j^2 \quad (30)$$

where  $\nu$  is the Poisson's ratio of the material,  $r_j$  is the maximum diameter of the jet, and  $r$  is the radius of any point inside the jet at a specific axial position. When  $r = 0$ , the two stress values mentioned above reach their maximum values. In line with engineering application requirements, this study will focus only on the maximum stress at each axial position of the jet. By substituting Equation 28 into the above expressions, we obtain:

$$\sigma_r = \sigma_c = \frac{3-2\nu}{8(1-\nu)} \rho_j \frac{R^4}{r_j^2} \Omega^2 \quad (31)$$

The above inequality represents the fracture condition for the rotating jet. To solve for the principal stresses and principal directions under the three-dimensional stress conditions, Wang [31] derived the corresponding formulas for the variables. Initially, the three stress invariants are listed as follow:

$$\begin{aligned} I_1 &= \sigma_x + \sigma_y + \sigma_z \\ I_2 &= \sigma_x \sigma_y + \sigma_y \sigma_z + \sigma_z \sigma_x - \tau_{xy}^2 - \tau_{yz}^2 - \tau_{xz}^2 \\ I_3 &= \sigma_x \sigma_y \sigma_z + 2\tau_{xy} \tau_{yz} \tau_{xz} - \sigma_x \tau_{yz}^2 - \sigma_y \tau_{zx}^2 - \sigma_z \tau_{xy}^2 \end{aligned} \quad (32)$$

and:

$$\begin{aligned} p &= \frac{3I_2 - I_1^2}{3} \\ q &= \frac{9I_1 I_2 - 2I_1^3 - 27I_3}{27} \end{aligned} \quad (33)$$

Finally, the three principal stresses can be derived [31]:

$$\begin{aligned}\sigma_1 &= \frac{I_1}{3} + 2\sqrt{-\frac{P}{3}} \cos \frac{\theta}{3} \\ \sigma_2 &= \frac{I_1}{3} - \sqrt{-\frac{P}{3}} \left( \cos \frac{\theta}{3} - \sqrt{3} \sin \frac{\theta}{3} \right) \\ \sigma_3 &= \frac{I_1}{3} - \sqrt{-\frac{P}{3}} \left( \cos \frac{\theta}{3} + \sqrt{3} \sin \frac{\theta}{3} \right)\end{aligned}\quad (34)$$

where  $\theta$  represents the principal direction angle, which can be calculated using Equation 35.

$$\theta = \arccos \left( -\frac{q}{2} \left( -\frac{P}{27} \right)^{-0.5} \right), \quad 0 \leq \theta \leq \pi \quad (35)$$

Then, according to the formula for principal strains in material mechanics [32], Equations 36 can be derived.

$$\begin{aligned}\varepsilon_1 &= \frac{1}{E} \left[ \sigma_1 - \nu(\sigma_2 + \sigma_3) \right] \\ \varepsilon_2 &= \frac{1}{E} \left[ \sigma_2 - \nu(\sigma_1 + \sigma_3) \right] \\ \varepsilon_3 &= \frac{1}{E} \left[ \sigma_3 - \nu(\sigma_1 + \sigma_2) \right]\end{aligned}\quad (36)$$

Since the jet remains in a plastic state during elongation [33], the tangent modulus  $E_{\text{tan}}$  is used in place of the elastic modulus  $E$  for this calculation. The material's equivalent strain is then calculated as:

$$\varepsilon_{eq} = \sqrt{\frac{2}{9} \left[ (\varepsilon_1 - \varepsilon_2)^2 + (\varepsilon_1 - \varepsilon_3)^2 + (\varepsilon_2 - \varepsilon_3)^2 \right]} \quad (37)$$

The condition for jet fracture occurs when the equivalent strain of a jet element exceeds the dynamic failure strain of the material, described as:

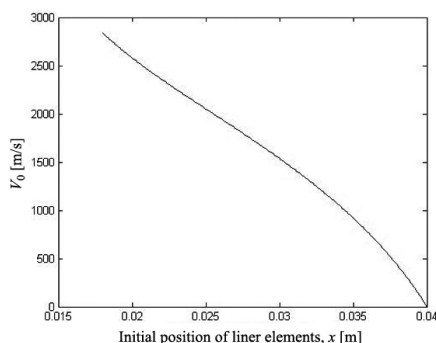
$$\varepsilon_{eq}(x, t) > \varepsilon_f(x, t) \quad (38)$$

### 3 Results and Discussion

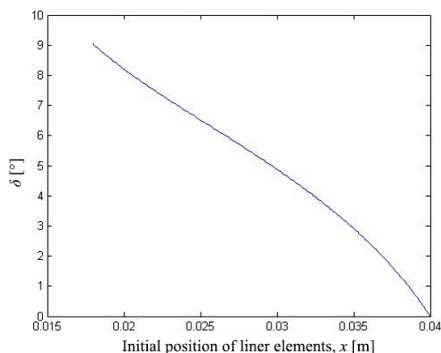
#### 3.1 Rotating jet axial velocity distribution

Using the theoretical formula outlined above, the crushing velocity distribution of the liner was calculated based on the charge structure shown in Figure 4. In this calculation, the charge adopts data for a Comp-B explosive (a Gruneisen energy of 3,672,050 J/g [34], detonation velocity of 7980 m/s and an initial density of 1.717 g/cm<sup>3</sup> [24]). The liner material was high-conductivity oxygen-free copper, and the material parameters are found in [24].

The relationship between the initial positions of the elements and the liner's initial crushing velocity  $V_0$ , with the origin at the initiation point, was calculated and is presented in Figure 10. Based on Equation 12, the distribution of the projection angle  $\delta$  with respect to  $x$  was obtained, as shown in Figure 11.

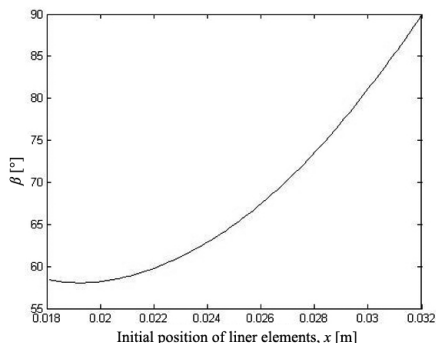


**Figure 10.** Distribution pattern of  $V_0$  with the initial position of each element

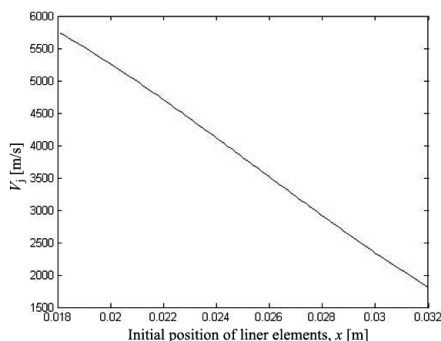


**Figure 11.** Distribution of the projection angle  $\delta$  with respect to  $x$

The effective crushing angle refers to the angle formed between the liner elements that can reach the x-axis [35]. Therefore, in these calculations, this study excludes liner elements that do not reach the axis. The resulting distribution pattern of the crushing angle is shown in Figure 12. The centrifugal and tangential stresses in the rotating jet alter its stress and strain states, thereby influencing the jet formation characteristics. This study establishes an analysis model of the liner (Figure 8) and selects a jet element at a specific position to derive the relationship between the angular velocity changes of this element before and after formation under rotation. Consequently, the distribution of the jet velocity with respect to the initial position  $x$  of the jet element was obtained, as illustrated in Figure 13.



**Figure 12.** Distribution of the crushing angle  $\beta$  with respect to  $x$

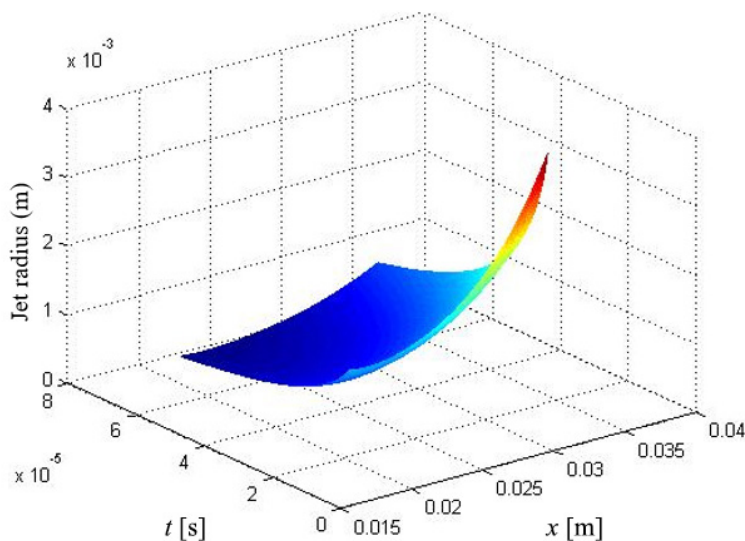


**Figure 13.** Distribution of the jet velocity  $V_j$  with respect to  $x$

The deviation between the jet tip velocity results shown in Figure 13 and the simulation results shown in Figure 7 was 4.2%, revealing a good consistency between the mentioned results. As seen from Figure 13, a velocity gradient exists between the tip and the tail of the jet after formation, which causes a gradual decrease in jet radius during elongation. This reduction in radius increases the centrifugal stress, influencing the jet's shaping process.

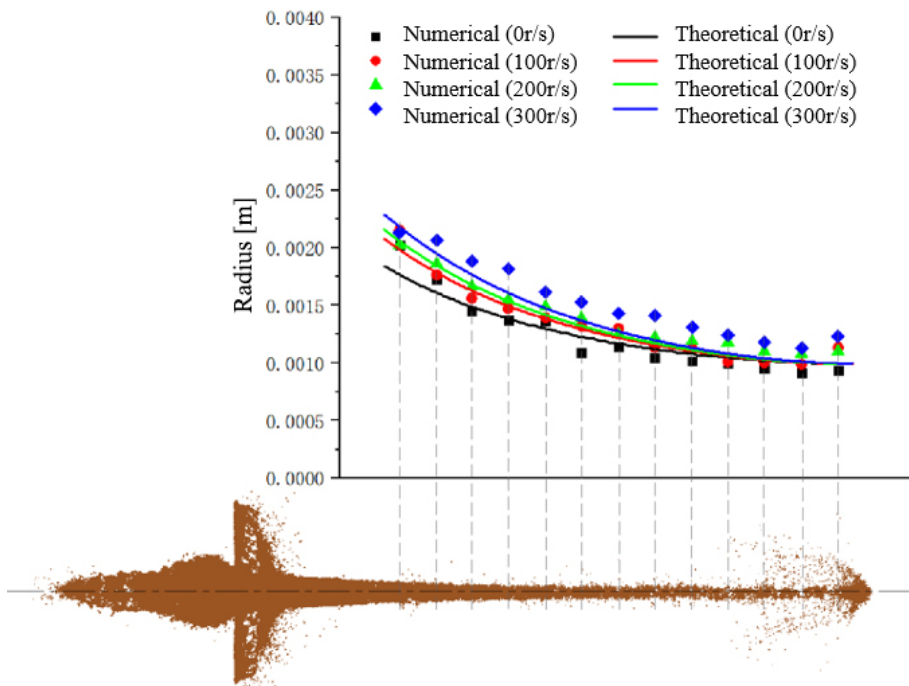
### 3.2 Rotating jet radius distribution

Figure 14 presents the distribution of the jet radius with respect to the initial position at different times  $t$ . The figure shows that the jet radius formed from the top to the bottom of the liner gradually increases, while the overall trend of the jet radius decreases over time. Based on the results in Figure 14, the radius variation of the rotating jet can be theoretically predicted.



**Figure 14.** Distribution of the jet element radius over time  $t$

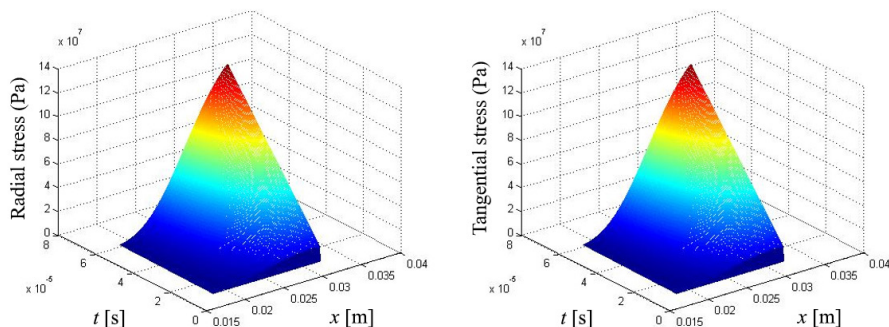
In order to validate the theoretical calculation results of the rotating jet radius, measurements were conducted on the numerical simulation results of the rotating jet. During this process, only the effective part of the jet, as shown in Figure 13 (with an axial velocity greater than or equal to 1800 m/s), was considered. Following the method outlined in reference [36], the jet boundary was extracted, and the jet diameter was measured at different positions along the axis. Finally, the jet radius at 25  $\mu$ s was statistically analysed and compared with the theoretical results, as illustrated in Figure 15.



**Figure 15.** Theoretical calculation results and numerical simulation results of the rotating jet radius

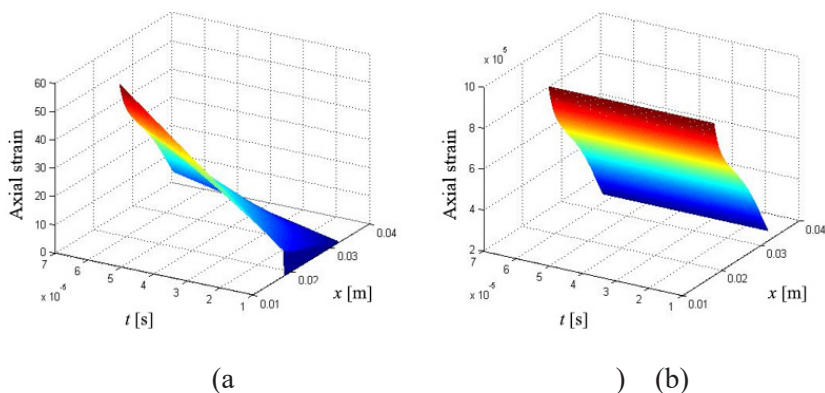
This figure demonstrates a close match between the theoretical calculations and the numerical simulation results for the rotating jet radius, validating the predictive model of the jet's radial morphology. Next, a theoretical analysis of the stress distribution in the rotating jet is conducted.

As an example, this study uses an initial angular velocity of  $\Omega = 100$  r/s to calculate the radial and tangential stress distributions of the jet with respect to the initial position  $x$  of the liner element at time  $t$ , as illustrated in Figure 16.



**Figure 16.** Distribution of the radial and tangential stresses of the jet with respect to the initial position of the liner element

The results indicate that the radial and tangential stresses within the jet increase over time, with the maximum stresses occurring in the jet formed at the bottom of the liner element. The strain and strain rate distributions of the jet, calculated from Equations 20 and 21 are shown in Figure 17.



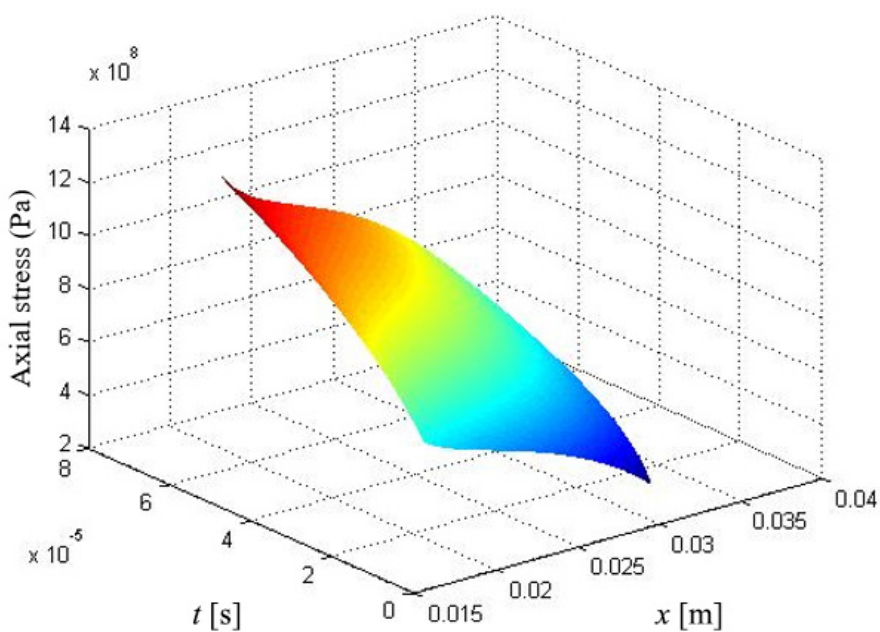
**Figure 17.** Distributions of the axial strain of the jet over time

According to the graph, if no fracture occurs during the jet formation process, the strain at the tip of the jet can reach 55, and the strain rate can reach  $9.4 \times 10^5$  after  $60 \mu\text{s}$ . Beyond strain and strain rate, temperature variation also influences the axial stress during jet formation.

Studies indicate that the temperature can be considered approximately uniform throughout the jet elongation process [37]Cu–Cr–Zr alloy liners fabricated by selective laser sintering process were deformed by explosive



detonation. Their as-manufactured (liner. Specifically, when using a Comp-B explosive and a high-conductivity oxygen-free copper liner, the jet's average temperature during formation ranges between 701 and 810 K [38]. Thus, in this theoretical analysis, the jet temperature was assumed to be uniformly distributed, with a post-formation temperature of 750 K [37]Cu–Cr–Zr alloy liners fabricated by selective laser sintering process were deformed by explosive detonation. Their as-manufactured (liner. This temperature was substituted into Equation 4 to calculate the jet's axial stress, and the resulting axial stress distribution is shown in Figure 18.

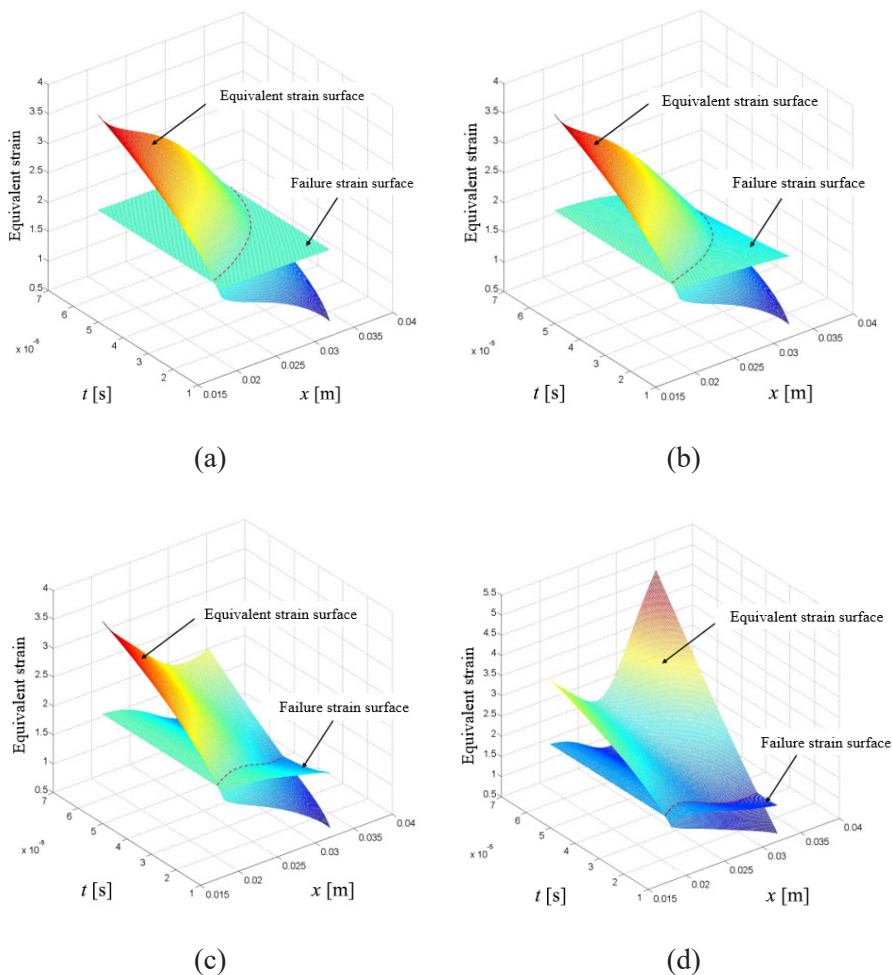


**Figure 18.** Distribution of the axial stress of the jet over time

The jet formed at the top of the liner exhibits the maximum axial stress due to the significant velocity gradient at the jet tip, which results in higher strain and strain rates. Considering the stress variations in different directions, this study calculates the equivalent strain and dynamic failure strain of the jet at various time intervals in order to estimate the fracture time of the rotating jet.

### 3.3 Effect of the initial angular velocity on the jet breakup time

The axial strain and the failure strain of each jet element at time  $t$  are calculated for the cases where the initial angular velocity  $\Omega$  is 0, 100, 200, and 300 r/s within 60  $\mu$ s. The distribution along  $x$  is shown in Figure 19.



**Figure 19.** Equivalent strain and failure strain of the jet at different initial angular velocities 0 (a), 100 (b), 200 (c) and 300 r/s (d)

The dashed lines in the figures represent the intersection between the equivalent strain surface and the dynamic failure strain surface. Each point on the intersection corresponds to an  $(x, t)$  value on the liner, indicating the moment

when jet elements at the initial position  $x$  undergo fracture at time  $t$ . For instance, in Figure 19(a), the curve indicates the scenario with an initial angular velocity of  $\Omega = 0$ . The fracture initiates at the tip of the jet at  $15 \mu\text{s}$  and propagates towards the tail, culminating in a complete fracture at  $52.7 \mu\text{s}$ .

Figure 19(b) shows results for an initial angular velocity of  $\Omega = 100 \text{ r/s}$ . Fracture at the jet tip occurs at  $14.3 \mu\text{s}$  and is complete by  $42 \mu\text{s}$ . Comparing these results with those in Figure 19(a) reveals that, while the equivalent strain surfaces are similar in shape, the failure strain surface in Figure 19(b) appears steeper. This suggests that rotation primarily affects jet fracture by altering its failure strain, with rotational forces introducing tangential and radial stresses that increase material stress triaxiality and thus accelerate failure.

When the initial angular velocity rises to  $200 \text{ r/s}$ , as shown in Figure 19(c), the jet's equivalent strain surface steepens, shortening the fracture propagation time. Measurements indicate that the fracture at the tip of the jet occurs at  $13.3 \mu\text{s}$  and is complete by  $29.5 \mu\text{s}$ .






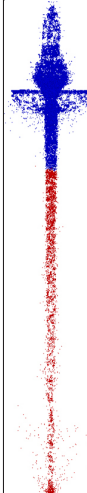

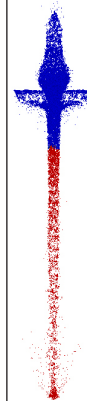
A similar phenomenon is observed in Figure 19(d), but with a distinct feature: the equivalent strain surface increases abruptly at the jet's tail. This increase is due to the larger radial and tangential stresses at the tail when no fracture occurs. At  $\Omega = 300 \text{ r/s}$ , fracture at the tip of the jet begins at  $13.0 \mu\text{s}$ , and is complete  $18.8 \mu\text{s}$  later.

Next, these results were validated using the previously described numerical simulation model, computing the jet formation morphology for initial angular velocities of  $0, 100, 200,$  and  $300 \text{ r/s}$ . The onset and completion times of jet fracture under each condition were calculated and compared with the theoretical results.

To identify fracture, the equivalent stress distribution is examined. However, since the numerical simulations output is discrete, it is challenging to capture the precise moment of fracture. Therefore, the equivalent stress contours at the moment of fracture were not shown. Once the equivalent stress drops to zero, fracture begins and jet fragmentation starts to increase. By the point at which jet fragmentation no longer increases, beyond an axial velocity threshold of  $1800 \text{ m/s}$ , it is considered that fragmentation has ended.

Table 4 presents both the theoretical and numerical results for the onset and completion times of jet fracture. Jet morphology is displayed using axial velocity contours, highlighting regions with axial velocities exceeding  $1800 \text{ m/s}$ . Red areas in the contours represent jet segments with axial velocities above this threshold.

**Table 4.** The numerical simulation results of the rotating jet fracture times are consistent with the theoretical analysis results

$\Omega$	0 r/s		100 r/s		200 r/s		300 r/s	
	breakup begins	breakup ends	breakup begins	breakup ends	breakup begins	breakup ends	breakup begins	breakup ends
Jet appearance								
Numerical result [ $\mu\text{s}$ ]	16	50	14	38	15	32	15	23
Theoretical result [ $\mu\text{s}$ ]	15	52.7	14.3	42	13.3	29.5	13	18.8
Deviation [ $\mu\text{s}$ ]	+1	-2.7	+0.3	-4	+1.7	+2.5	+2	+4.2

The results indicate that the deviation between the theoretical analysis and the numerical simulation results remains within  $\pm 4 \mu\text{s}$ , with a minimum deviation of only  $0.3 \mu\text{s}$ , validating the accuracy of the theoretical calculations proposed in this study.

Additionally, Table 4 shows that, across different initial angular velocities, the onset time of jet fragmentation remains relatively consistent. This stability arises from the minimal diameter variation of the jet tip before and after formation, meaning that rotation has little effect on the jet tip formation process. However, as the initial angular velocity is increased, the time interval between the onset and completion of fragmentation shortens, indicating that the jet fragments more quickly into multiple pieces.

## 4 Conclusions

This paper initially conducted numerical simulation studies on the formation of rotating jets, revealing the correlation between the axial and tangential motions of the jet. Building on these findings, a theoretical analysis of rotating jet formation characteristics was performed, with a systematic examination of jet morphology and fracture phenomena under rotational conditions. Numerical simulation results were then used to validate the theoretical analysis. The following regularities were identified:

- ◆ The angular velocity of rotating jets has a negligible effect on axial velocity, allowing the independent study of axial and tangential motions in theoretical models.
- ◆ The predicted jet radius and tip velocity from the theoretical model closely match the numerical simulation results, validating both the rationality of the hypotheses and the accuracy of the proposed theoretical model.
- ◆ Regardless of the initial angular velocity, jet fracture does not occur instantaneously but propagates from the tip to the tail.

## Acknowledgments

This research was funded by the National Key Laboratory of Explosion Science and Safety Protection (Beijing Institute of Technology), grant number YBKT23-09.

## References

- [1] Simon, J.; Martin, T.H. *Spin Compensation of Shaped Charge Liners Manufactured by the Rotary Extrusion Process*. Aberdeen Proving Ground, MD, BRL Memo. Rep., **1958**.
- [2] Segletes, S.B. *Mechanisms Inducing Jet Rotation in Shear-formed Shaped-Charge Liners*. US Army Ballistic Research Laboratory, Aberdeen Proving Ground, MD, Report No. BRL-TR-3090, **1990**.
- [3] Vladilen, F.M.; Igor, V.M.; Oleg, V.M. The Brief Review and Experimental Verification of Possibility of Spin Compensation Losses in Explosive Shaped Charge by Magnetic Field. *Int. J. Mod. Appl. Phys.* **2013**, *3*(1): 1-7.
- [4] Singh, S. Penetration of Rotating Shaped Charges. *J. Appl. Phys.* **1960**, *31*(3): 578-581; <https://doi.org/10.1063/1.1735631>.
- [5] Segletes, S.B. *Mechanisms Inducing Jet Rotation in Shear-formed Shaped-Charge Liners*. Master Dissertation, Drexel University, **1988**.
- [6] Ugrčić, M.; Maksimović, S. Critically Shaped Charge Jet Stress Caused by Angular

- Velocity. *Facta Univ., Ser.: Mechanics, Automatic Control and Robotics* **2007**, 6(1): 119-130.
- [7] Li, R.J.; Lu, Z.Y.; Fang, Z.J.; Sun, S.J. Numerical Simulation of Rotational Velocity on Shaped-Charge Jet Formation. *J. Projectiles, Rockets, Missiles Guidance* **2013**, 33(5): 99-102.
- [8] Men, J.B.; Jiang, J.W.; Wang, S.Y. *Fundamentals of Numerical Simulation for Explosion and Shock Problems*. Beijing: Beijing Institute of Technology Press, **2015**; ISBN 978-7-5682-0919-9.
- [9] Duan, Y.; Zhao, Y.Z.; Ren, H.L. Numerical Study on the Fracture Characteristics of Projectile Material under Impact Loading. (in Chinese) *Sci. Sin. Tech.* **2016**, 46: 357-367; <https://doi.org/10.1360/N092016-00006>.
- [10] An, X.Y.; Dong, Y.X.; Liu, J.Y.; Tian, C. General Formula to Calculate the Fragment Velocity of Warheads with Hollow Core. *Int. J. Impact Eng.* **2018**, 113: 1-8; <https://doi.org/10.1016/j.ijimpeng.2017.11.006>.
- [11] Feng, D.L.; Liu, M.B.; Li, H.Q.; Liu, G.R. Smoothed Particle Hydrodynamics Modeling of Linear Shaped Charge with Jet Formation and Penetration Effects. *Comput. Fluids* **2013**, 86: 77-85; <https://doi.org/10.1016/j.compfluid.2013.06.033>.
- [12] Qiang, H.F.; Wang, K.P.; Gao, W.R. Numerical Simulation of Shaped Charge Jet using multi-Phase SPH Method. *Trans. Tianjin Univ.* **2008**, 14(1): 495-499; <https://doi.org/10.1007/s12209-008-0084-9>.
- [13] Gustafsson, A. *Shaped Charge Design: Construction of a Miniaturized Shaped Charge*. Karlstads University, **2021**.
- [14] Hallquist, J.O. *Theoretical Manual for DYNA3D*. Lawrence Livermore National Lab., **1983**, US-CA.
- [15] Chokshi, A.H.M.M. The Prospects for Superplasticity at High Strain Rates Preliminary Considerations and an Example. *Scr. Metall. Mater.* **1990**, 24(4): 605-610; [https://doi.org/10.1016/0956-716X\(90\)90209-Y](https://doi.org/10.1016/0956-716X(90)90209-Y).
- [16] Yan, C.; Huang, Z.X.; Zu, X.D.; Xiao, Q.Q.; Jia, X. Ultra-fine Grained Pure Copper Shaped Charge Liner Performance Study. **2017**, 36(3): 72-76; <https://doi.org/10.7690/bgzd.2017.03.019>.
- [17] Liu, G.R.; Liu, M.B.; Han, X.; Yang, G.; Qiang, H.F. *Smoothed Particle Hydrodynamics: a Meshfree Particle Method*. Hunan/Changsha: Hunan University Press, **2005**; ISBN: 7-81053-998-1.
- [18] Silvestrov, V.V.; Gorshkov, N.N. Effect of the Strain Rate on the Tensile Strength of a Copper Shaped-Charge Jet. *Combust., Explos. Shock Waves* **1997**, 33(1): 93-99. <https://doi.org/10.1007/BF02671859>.
- [19] Lee, E.L.; Hornig, H.C.; Kury J.W. *Adiabatic Expansion of High Explosive Detonation Products*. University of California Radiation Lab., Livermore, Livermore, US-CA, **1968**.
- [20] Cudzilo, S.; Trzcinski, W.A. A Study on Detonation Characteristics of Pressed NTO. *J. Energ. Mater.* **2001**, 19(1): 1-21; <https://doi.org/10.1080/07370650108219390>.
- [21] Johnson, G.R.; Cook, W.H. Fracture Characteristics of Three Metals Subjected to Various Strains, Strain Rates, Temperatures and Pressures. *Eng. Fract. Mech.*

- 1985, 21(1): 31-48; [https://doi.org/10.1016/0013-7944\(85\)90052-9](https://doi.org/10.1016/0013-7944(85)90052-9).
- [22] Pappu, S.; Murr, L.E. Hydrocode and Microstructural Analysis of Explosively Formed Penetrators. *J. Mater. Sci.* **2002**, 37: 233-248; <https://doi.org/10.1023/A:1013665108127>.
- [23] Huang, X.C; Chen, Y.Z.; Zhu, J.S. Method for Determining Material Failure Function in Notched Specimen Tensile Test. *Chin. J. Solid Mech.* **2008**, 29(4): 385-388.
- [24] Xin, C.L.; Xue, Z.Q.; Tu, J.; Wang, X.Q.; Sun, F.T.; Shi, D.Y. *Parameter Manuals for Common Materials used in Finite Element Analysis*. Beijing: China Machine Press, **2020**; ISBN 978-7-111-64294-7.
- [25] Chou, P.C.; Flis, W.J. Recent Developments in Shaped Charge Technology. *Propellants Explos. Pyrotech.* **1986**, 11(4): 99-114; <https://doi.org/10.1002/prop.19860110402>.
- [26] Gurney, R.W. *The Initial Velocities of Fragments from Bombs, Shell, Grenades*. Aberdeen Proving Ground, MD: Ballistic Research Laboratories, **1943**.
- [27] Chanteret, P.Y. An Analytical Model for Metal Acceleration by Grazing Detonation *Proc. 7<sup>th</sup> Int. Symp. Ballistics*, **1983**, 515-524.
- [28] Zhang, B.P.; Zhang, Q.M.; Huang, F.L. *Detonation Physics*. Beijing: Ordnance Industry Press, **2001**.
- [29] Pugh, E.M.; Eichelberger, R.J.; Rostoker, N. Theory of Jet Formation by Charges with Lined Conical Cavities. *J. Appl. Phys.* **1952**, 23(5): 532-536; <https://doi.org/10.1063/1.1702246>.
- [30] Cheng, D.X. *Mechanical Design Manual. Commonly used Design Materials*. Beijing: Chemical Industry Press, **2004**.
- [31] Wang, K. Calculation Formulas for Principal Stresses. *Mech. Eng.* **2014**, 36(6): 783-785; <https://doi.org/10.6052/1000-0879-13-502>.
- [32] Han, B.; Liu, H.Y.; Shui, X.P. *Mechanics of Materials Tutorial*. Beijing: Publishing House of Electronics Industry, **2013**.
- [33] Murr, L.E.; Trillo, E.A.; Pappu, S.; Kennedy, C. Adiabatic Shear Bands and Examples of Their Role in Severe Plastic Deformation. *J. Mater. Sci.* **2002**, 37: 3337-3360; <https://doi.org/10.1023/A:1016541023502>.
- [34] James, E.K. *The Gurney Model of Explosive Output for Driving Metal. Explosive Effects and Applications*. New York: Springer New York, **1998**, pp. 221-257.
- [35] Huang, Z.X. *Theory and Practice of Shaped Charge*. Beijing: Beijing Institute of Technology Press, **2014**.
- [36] Sun, S.J.; Wang, S.Y.; Tan, J.; Jiang, J.W.; Men, J.B. Numerical Simulation of the Influence Factors on the Forming Performance of Explosively Formed PELE. *Chin. J. Explos. Propellants* **2020**, 43(3): 325-329; <https://doi.org/10.14077/j.issn.1007-7812.201909027>.
- [37] Agu, H.O.; Hameed, A.; Appleby-Thomas, G.J. Comparison of the Microstructure of Machined and Laser Sintered Shaped Charge Liner in the Hydrodynamic Regime. *J. Dynamic Behavior Mater.* **2019**, 5: 484-494; <https://doi.org/10.1007/s40870-019-00213-y>.

- [38] von Holle, W.G.; Trimble, J.J. Temperature Measurement of Shocked Copper Plates and Shaped Charge Jets by Two-Color IR Radiometry. *J. Appl. Phys.* **1976**, *47*(6): 2391-2394; <https://doi.org/10.1063/1.323028>.

**Contribution:**

Shengjie Sun: conception, methods, performing statistical analysis

Shuyou Wang: conception

Jianwei Jiang: methods

Zhaoting Li: performing statistical analysis

Hang Yang: performing statistical analysis

Jianbing Men: foundations

Received: May 10, 2024

Revised: December 20, 2024

First published online: December 20, 2024